Journal of Materials Chemistry A

PAPER

View Article Online
View Journal | View Issue





Cite this: *J. Mater. Chem. A*, 2019, **7**, 16304

# Introducing pyridyl into electron transport materials plays a key role in improving electron mobility and interface properties for inverted perovskite solar cells†

Rui Zhu, Quan-Song Li* and Ze-Sheng Li*

Received 9th May 2019
Accepted 12th June 2019

DOI: 10.1039/c9ta04856a

rsc.li/materials-a

In inverted perovskite solar cells (PSCs), electron transfer materials (ETMs) have a significant effect on the efficiency and stability, because they can reduce the energy barrier between the perovskite film and electrode materials and suppress the potential interfacial charge recombination. Herein we designed a series of ETMs (*o*-PDTP, *m*-PDTP, and *p*-PDTP) through introducing pyridyl as the side chain of the experimentally synthesized ETM 10,14-bis(5-(2-ethylhexyl)thiophen-2-yl)-dipyrido-[3,2-*a*:2′,3′-*c*][1,2,5]-thiadiazolo-[3,4-*i*]-phenazine (TDTP) based on quantum chemical calculations. Our results showed that introducing pyridyl changes the molecular packing mode from the herringbone packing motif in TDTP to two-dimensional π–π stacking in *p*-PDTP due to the strong interactions between the added nitrogen atoms and the hydrogen atoms of the molecular skeleton. Therefore, the average electron mobility of *p*-PDTP (1.65 $cm^2\ V^{-1}\ s^{-1}$) is 34 times higher than that of TDTP. Our results also indicated that the additional N⋯Pb interface interaction between the nitrogen atoms in the ETMs and the lead atom in $MAPbI_3$ leads to stronger binding energies and easier electron injection. The present results not only offer two promising ETMs (*m*-PDTP and *p*-PDTP), but also propose a new design strategy of introducing pyridyl into ETMs for more efficient PSCs.

## Introduction

Inverted perovskite solar cells with the device structure of indium tin oxide/hole transfer layer/perovskite active layer/electron transfer layer/metal electrode have been rapidly pursued because of their negligible hysteresis, low temperature processing, and device structure flexibility.[1–4] Suitable electron transfer materials (ETMs) contribute greatly to less hysteresis, higher current density, and lower recombination kinetics.[5,6] Compared with the rapid development of hole transfer materials (HTMs), relatively few ETMs were reported. Metal oxides like $TiO_2$ used in conventional type PSCs as ETMs require high temperatures (up to 500 °C), which makes the fabrication process complicated.[7] Fullerenes and their derivatives have been widely used in inverted PSCs as ETMs, while they suffer from certain drawbacks such as high cost, difficulty in fabricating thick dense films, and relatively poor temporal stability.[8] Therefore, developing new non-fullerene ETMs to overcome the aforementioned disadvantages while promoting the favorable properties becomes one of the top priorities for advancing the efficiency and stability of PSCs.

Electron transport involving ETMs of PSCs mainly consists of two parts: transport between the perovskite and ETM and transport in the ETM. For the first part, many studies have been performed through introducing an interfacial modifier layer between the perovskite and ETM (such as INIC series, B2F, C-HATNA, and ITIC), which can promote the formation of high quality and uniform perovskite films, passivate defects, improve the interface interaction between the perovskite and ETM, and enhance electron extraction, resulting in improved PSC performance.[9–13] Some research groups have tried to modify ETMs by introducing some functional groups which can form interaction between the perovskite and ETM, such as amino groups, pyridyl, thiophene, and halogen atoms.[14–18] For the second part, great efforts have been devoted to improving the electron mobility in ETMs since higher electron mobility decreases the possibility of electron accumulation and recombination.[19] The electron mobility of semiconductor materials can be improved by introducing various heteroatoms (nitrogen, sulfur, and so on) or extending the π-conjugation.[20,21] So designing ETMs with

*Key Laboratory of Cluster Science of Ministry of Education, Beijing Key Laboratory of Photoelectronic/Electrophotonic Conversion Materials, School of Chemistry and Chemical Engineering, Beijing Institute of Technology, 100081 Beijing, China. E-mail: liquansong@bit.edu.cn; zeshengli@bit.edu.cn*

† Electronic supplementary information (ESI) available: Computational details, the structures and energies of the studied compounds, interactions between molecules, and the interface properties with the MA-terminated perovskite surface. See DOI: 10.1039/c9ta04856a

a stronger perovskite/ETM interface interaction and higher electron mobility has proved to be an effective way to achieve more efficient PSCs.

Pyridine type compounds have attracted wide attention for their application in enhancing the efficiency of PSCs. As a base, pyridyl can donate its lone pair electrons in the nitrogen atom to Lewis acids. In addition, pyridyl has a planar geometry with aromaticity, so adding pyridyl into ETMs increases the length of the conjugated part and retains the aromaticity. There are several ways of introducing pyridyl or its derivatives into PSCs. First, pyridinium type compounds (such as 4-tert-butylpyridine) have been used as additives in perovskite films to obtain high quality perovskite layers.[22,23] Due to the strong coordination between the nitrogen atom at the end of 4-tert-butylpyridine and the $Pb^{2+}$ in $MAPbI_3$, they can suppress perovskite nucleation by forming an intermediate phase. Second, pyridine type compounds (for example, 4-picolinic acid) were used as interfacial modifier layers, in which pyridyl groups were anchored on the surface of perovskite layers owing to strong electron coupling between the ETM and perovskite to facilitate charge carrier transport and suppress interfacial charge recombination.[24] Furthermore, Yang and co-workers reported C60-Py as an ETM, where pyridyl was anchored onto the perovskite film, thus reinforcing the passivation of the trap states within the $MAPbI_3$ perovskite film and suppressing the nonradiative electron–hole recombination, leading to enhanced electron transport reflected by the increase of short-circuit current density ($J_{sc}$).[25] In addition, pyridyl groups have been developed to tune the energy level and improve electron mobility, where the position of nitrogen has a significant effect on those properties.[26–29] Inspired by the above work, we propose an idea of introducing pyridyl into ETMs to improve the interface interaction between the perovskite and ETM and enhance the electron mobility within ETMs.

n-Type small molecule TDTP used as an ETM reported by the Zhang group exhibited an impressive power conversion efficiency (PCE) of 18.2%, which is ranked among the high PCEs,[30,31] while compared to the conventional device which has a PCE of up to 23.7%, there is still some room to improve.[32] On analysis of the two devices we found that the main difference in PCE comes from the $J_{sc}$ and the fill factor (FF). Previous reports have proved that the higher electron mobility of the ETM contributes to the increase of $J_{sc}$ and FF,[33] while the electron mobility of TDTP is smaller than that of $TiO_2$.[34] Therefore, taking the above factors into account, in this work, we introduced pyridyl into TDTP, and thus designed three new ETM molecules (*o*-PDTP, *m*-PDTP, and *p*-PDTP), varying in the position of the nitrogen atom in the pyridyl, see Fig. 1. The electronic properties and electron mobility of TDTP and the newly designed ETM molecules, together with the corresponding perovskite/ETM interface features have been systematically studied based on first-principles calculations and Marcus theory. The computational details are given in the ESI.† Our obtained data show that introducing pyridyl is beneficial to increase the transfer mobility and interface interaction. We hope our work provides useful implications for future experimental synthesis.

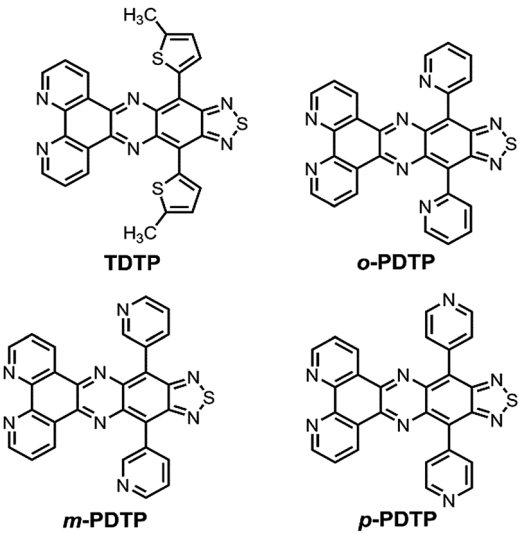


Fig. 1 The chemical structures of studied molecules.

## Results and discussion

### Geometric and electronic structures

Molecular geometry and frontier orbital characteristics are of importance to the packing mode and charge transfer efficiency.[35] Little difference in structure may cause a large change in mobility. We found that the geometric structures of the studied ETM molecules can be divided into two parts: the molecular skeleton and the side chains connected by a freely rotating single bond. To get more information about the geometries of the investigated molecules, the single bond was scanned using the B3LYP/6-31g(d,p) method and the results are shown in Fig. ESI1.† One can find that the energy fluctuation range (less than 5 kcal $mol^{-1}$) of TDTP with the dihedral angle between the molecular skeleton and side chain changing is smaller than that (more than 13 kcal $mol^{-1}$) of PDTPs. Starting from the two lowest energy points of the scan, we optimized the structures by the B3LYP method and re-calculated the energies at the CCSD/6-31g(d,p) level. The obtained structures with the lowest energy are displayed in Fig. 2 and the corresponding energies are given in Table ESI1.† In TDTP the side twist on the skeleton is 26°, while for *o*-PDTP the twist angle is 69°, resulting from the strong repulsion of the lone pair electrons of the nitrogen atoms in pyridyl and thiadiazole where the related distance is about 3.2 Å. These twist angles decrease to 52 and 53° in *m*-PDTP and *p*-PDTP, respectively, since the N···N distance increases to 5.0 Å in *m*-PDTP and 5.1 Å in *p*-PDTP. Clearly, introducing pyridyl into TDTP increases the twist angles, which decrease with the increase of the distance between the nitrogen atom of pyridyl and the molecular skeleton.

The energy levels of the highest occupied molecular orbital ($E_{HOMO}$) and the lowest unoccupied molecular orbital ($E_{LUMO}$) for all molecules calculated at the PBE33/6-31g(d,p) level of theory are presented in Fig. 3. The PBE33 functional has proved successful in describing the $E_{LUMO}$ of the TDTP family and

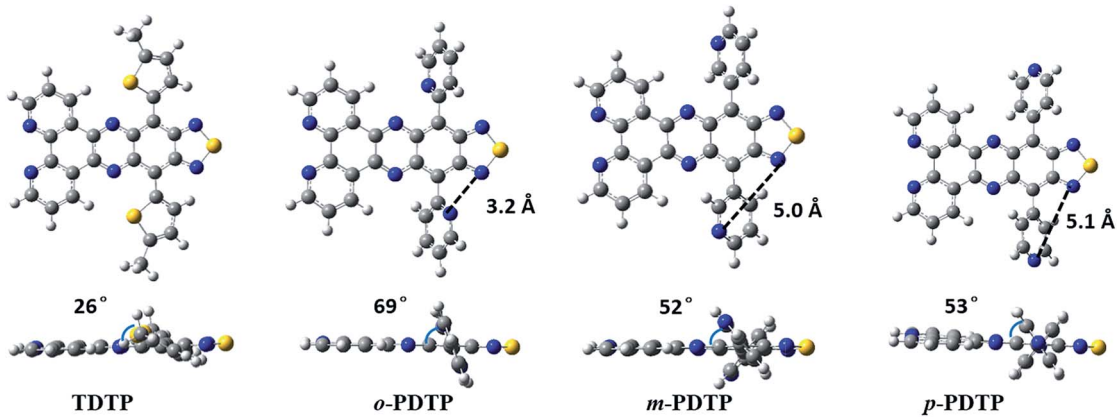


Fig. 2 The orthographic (up) and the side (down) views of optimized molecular geometries of the studied molecules, where the dashed lines indicate the N···N distances.

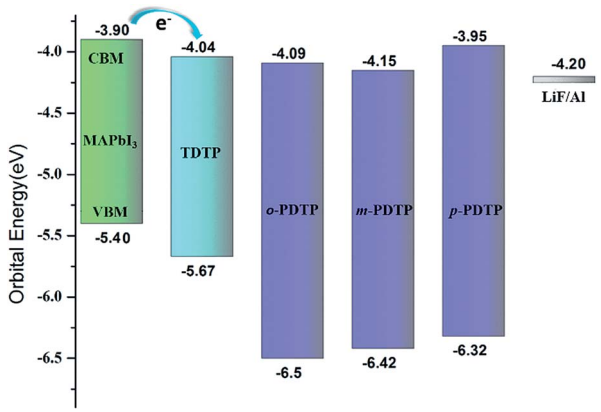


Fig. 3 Calculated HOMO and LUMO energy levels by the PBE33/6-31G(d,p) method for TDTP and the designed molecules, together with the CBM and VBM of $MAPbI_3$ and the work function of LiF/Al obtained from ref. 31.

similar organic compounds.[36,37] Here, all the molecular geometries were fully optimized at the PBE33/6-31g(d,p) level, and the time-dependent density functional theory (TDDFT) was used to simulate the excitation energies. The $E_{LUMO}$ was obtained using those $E_{HOMO}$ plus the first excitation energies.[38] As can be seen, the $E_{LUMO}$ of TDTP is −4.04 eV, which matches well with the experimental result of −4.03 eV.[31] The $E_{LUMO}$ values of the newly designed molecules are in the range of −3.95 eV to −4.15 eV, which are lower than the conduction band minimum (CBM) of −3.90 eV in $MAPbI_3$, ensuring electron transfer from the $MAPbI_3$ to ETM. In addition, the $E_{LUMO}$ values of the newly designed molecules are larger than the work function of LiF/Al (−4.20 eV) that has been often used as the metal electrode, which ensures that the electron can transfer to the electrode without energy barriers.[39] On the other hand, the $E_{HOMO}$ values of PDTPs are lower than the valence band maximum (VBM) of −5.40 eV in $MAPbI_3$, meaning that the hole transfer is prevented effectively. Note that the HOMO–LUMO energy gaps around 2.3 eV in PDTPs are larger than 1.63 eV in TDTP, meaning that PDTPs are conducive to prohibiting the recombination of holes and electrons in the ETMs. The above results indicate that the newly designed molecules may possess suitable energy levels as ETMs to combine with $MAPbI_3$ and the LiF/Al electrode at the monomolecular level.

In addition, the device instability is also the limitation factor for the application of PSCs. When formed on the top of the perovskite layer, the ETM also acts as the first protection layer for the perovskite material against oxygen, moisture, and heat.[40] Some studies have shown that the main reason of instability is the decomposition of the perovskite induced by $H_2O$ and $O_2$, and the decomposition products $PbI_2$ or $I^-$ will go through the ETM layer to metal electrode and decrease the PCE.[41,42] Suitable ETMs are expected to work in resisting $H_2O$ and $O_2$. The adiabatic electron affinity ($EA_a$) is directly relevant to the anionic species stability toward the reaction with water and oxygen in air.[43,44] The absolute hardness ($\eta$) can express the resistance of the chemical potential to the change in the number of electrons.[45] So the $EA_a$ and $\eta$ are used to study the air stability, and the results are listed in Table 1. We can see that the $EA_a$ and $\eta$ values of the newly designed molecules are larger than those of TDTP, which may significantly improve the device operational stability compared to that using TDTP as the ETM.

A significant advantage of inverted PSCs over the conventional device is that they can be fabricated at low temperature because of the solution-processed n-type organic semiconductor used as the ETM rather than high temperature sintering/annealing inorganic metal oxides like $TiO_2$.[46,47] The higher solubility of ETMs in organic solvents is beneficial for

Table 1 The adiabatic ionization potential ($IP_a$, eV), adiabatic electron affinities ($EA_a$, eV), the absolute hardness ($\eta$, eV), and the solvation free energy ($\Delta G_{solv}$, kcal mol$^{-1}$) of the investigated molecules

| Compounds | $IP_a$ | $EA_a$ | $\eta$ | $\Delta G_{solv}$ |
|---|---|---|---|---|
| TDTP | 5.17 | 3.79 | 0.69 | −12.79 |
| *o*-PDTP | 6.08 | 3.80 | 1.14 | −15.88 |
| *m*-PDTP | 5.98 | 3.83 | 1.08 | −14.52 |
| *p*-PDTP | 6.18 | 3.90 | 1.14 | −15.12 |

 

improving the film-forming ability. According to the fabrication process of the TDTP-based ETMs, the solvation free energies ($\Delta G_{solv}$) of the studied molecules were calculated in 1,2-dichlorobenzene to keep the same as the experimental solvent. The $\Delta G_{solv}$ values were obtained by subtracting the energy of gas phases from the energy of the solute in the solution.[48] As shown in Table 1, the $\Delta G_{solv}$ values of PDTPs are more negative than that of TDTP, indicating that the newly designed molecules possess higher solubility than TDTP.

## Transport properties

Electron mobility is closely related to the $J_{sc}$ and FF of PSCs.[33] The hopping mechanism, in which the charge carriers likely localize on a molecule and charge random jumps between neighboring molecules, has proved successful in description of the organic semiconductor transporting mechanism.[49] Marcus-type expression, which is an appropriate choice and has been widely used to predict the electron mobility, was employed to evaluate the electron mobility using the MOMAP software package.[50,51] More details can be found in the Computational details part of the ESI.†

The calculated average mobility values and the related parameters are summarized in Table 2. The average electron mobility values are 0.048, 0.024, 0.056, and 1.65 $cm^2 V^{-1} s^{-1}$ for TDTP, *o*-PDTP, *m*-PDTP, and *p*-PDTP, respectively, where the mobility of *p*-PDTP is about 34 times higher than that of TDTP.

The reorganization energy ($\lambda$) mainly originates from the geometrical relaxation during the charge transfer process and reflects the barriers from one molecule to another.[52] The $\lambda$ values were estimated by the adiabatic potential energy surface approach at the B3LYP/6-31G(d,p) level,[53] and the obtained results are listed in Table 2. The $\lambda$ values of PDTPs are in the range of 0.18–0.21 eV, close to 0.19 eV for TDTP. The results show that the difference of $\lambda$ is too small to lead to a big difference in electron mobility.

Table 2 The reorganization energy $\lambda$ (eV), centroid to centroid distance $d$ (Å), the electron transfer integral $v$ (eV), electron hopping rate $k$ ($s^{-1}$), and average electron mobility ($\mu_e$, $cm^2 V^{-1} s^{-1}$)

| Compounds | $\lambda$ | Path | $d$ | $v$ | $\mu_e$ |
|---|---|---|---|---|---|
| TDTP | 0.19 | 1 | 12.52 | $-2.06 \times 10^{-3}$ | 0.048 |
| | | 2 | 12.81 | $4.54 \times 10^{-3}$ | |
| | | 3 | 4.02 | $-1.06 \times 10^{-2}$ | |
| | | 4 | 4.02 | $-1.06 \times 10^{-2}$ | |
| | | 5 | 12.52 | $-2.06 \times 10^{-3}$ | |
| | | 6 | 12.81 | $4.54 \times 10^{-3}$ | |
| *o*-PDTP | 0.21 | 1 | 14.41 | $-0.63 \times 10^{-3}$ | 0.024 |
| | | 2 | 12.62 | $1.18 \times 10^{-3}$ | |
| | | 3 | 3.86 | $-9.00 \times 10^{-3}$ | |
| | | 4 | 3.86 | $-9.00 \times 10^{-3}$ | |
| | | 5 | 11.97 | $-9.94 \times 10^{-3}$ | |
| | | 6 | 13.03 | $9.63 \times 10^{-3}$ | |
| *m*-PDTP | 0.18 | 1 | 13.58 | $-3.79 \times 10^{-3}$ | 0.056 |
| | | 2 | 12.55 | $-2.10 \times 10^{-3}$ | |
| | | 3 | 3.78 | $1.80 \times 10^{-2}$ | |
| | | 4 | 3.78 | $1.79 \times 10^{-2}$ | |
| | | 5 | 12.55 | $-2.10 \times 10^{-3}$ | |
| | | 6 | 13.58 | $-3.79 \times 10^{-3}$ | |
| *p*-PDTP | 0.20 | 1 | 13.62 | $-1.48 \times 10^{-4}$ | 1.65 |
| | | 2 | 6.76 | $-4.06 \times 10^{-2}$ | |
| | | 3 | 6.76 | $-4.06 \times 10^{-2}$ | |
| | | 4 | 8.62 | $-5.42 \times 10^{-2}$ | |
| | | 5 | 8.62 | $-5.41 \times 10^{-2}$ | |
| | | 6 | 13.62 | $-6.52 \times 10^{-3}$ | |

The transfer integral ($v$) reflects electronic coupling between the neighboring molecules and needs to be maximized in order to improve the electron transport process.[54] The transfer integral has been shown to be very sensitive to the relative position of the neighboring molecules.[55] The crystal structure offering the relative position of the molecules plays an essential role in electron transport. The polymorph module in Materials studio was used in prediction of the crystal structure (for details please see ESI†), which has been proven to be an appropriate method.[56,57] The main electron hopping pathways and the corresponding $v$ values of the investigated molecules are given in Fig. 4 and Table 2. We can see that the TDTP crystal possesses a herringbone packing motif with π–π overlap between adjacent molecules, while the crystals of *o*-PDTP and *m*-PDTP exhibit one-dimensional (1D) π–π stacking, and *p*-PDTP shows two-dimensional (2D) π–π stacking.

In TDTP, the largest values of $v$ appear in path 3 and path 4, where the molecules exhibit a face-to-face (π–π) stacking pattern, while the intermolecular interactions are not strong due to the large centroid-to-centroid distance of 4.02 Å. A similar situation is found in *m*-PDTP, although it adopts 1D π–π stacking, in which path 3 and path 4 present the biggest transfer integral ($1.80 \times 10^{-2}$ eV). We can see that the largest $v$ in *m*-PDTP is larger than that in TDTP, due to the smaller centroid-to-centroid distance of 3.78 Å than that in TDTP. There are some interesting points in *o*-PDTP, where the largest transfer integral appears in path 5 not path 3 and path 4, because of the larger displacements and weaker LUMO–LUMO overlap between the molecules in these two paths and the central molecule (please see Fig. ESI2†). The *p*-PDTP adopts a 2D π–π stacking, and the $v$ values around paths 2, 3, 4, and 5 are $4.06 \times 10^{-2}$ eV and $5.42 \times 10^{-2}$ eV, which are obviously larger than those in other molecules. The larger transfer integral is attributed to the perfect packing mode, where the central molecule overlaps with those molecules in paths 2, 3, 4, and 5, and the reasons of this packing will be further discussed below.

The electrostatic potential (ESP) has been used as an interpretative tool in the analysis of non-covalent interactions ruling the shape of a crystal packing.[58,59] As shown in Fig. 5, the negative potential is mainly located on the nitrogen atoms of the 2,9-phenanthroline (left side) part of the molecular skeleton terminal in TDTP, while the positive potential appears on the right side of the molecular skeleton and side chains. The maximum electrostatic attraction usually appears between the positive potential and negative potential, so TDTP exhibits a herringbone packing motif thanks to the skeleton (left side)-skeleton (right side) and skeleton (left side)-side chain attractions. In PDTPs, the negative potential changes following the position change of the nitrogen atom in the pyridyl. In *o*-PDTP and *m*-PDTP, the negative potential also appears in the side chains near the molecular skeleton, so the electrostatic

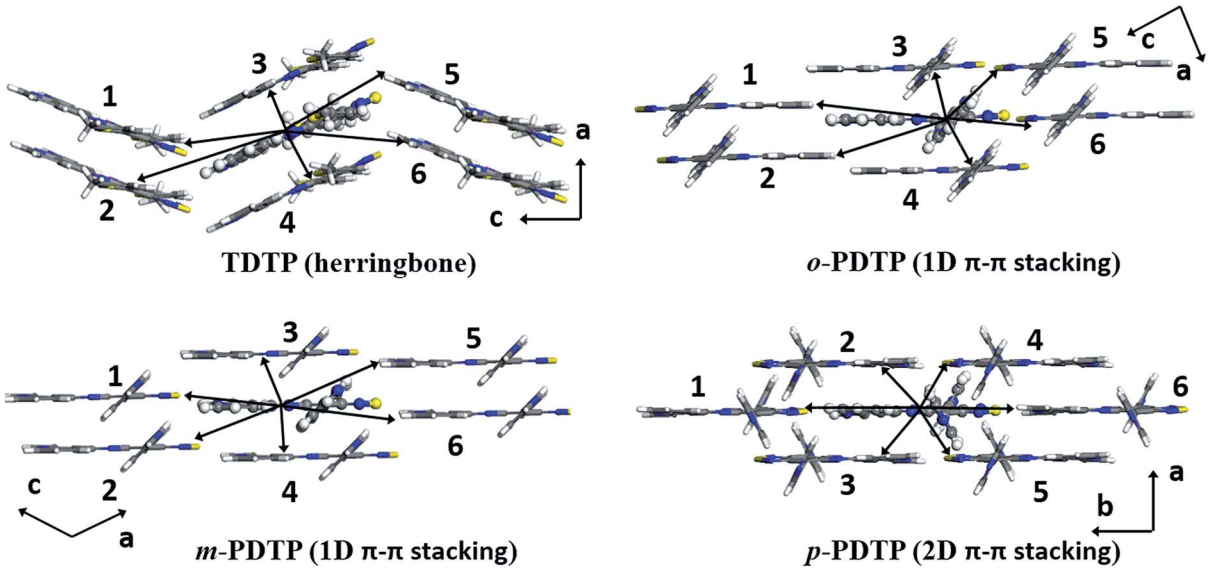


Fig. 4 Schemes of main electron hopping pathways in the predicted crystals with the packing mode.

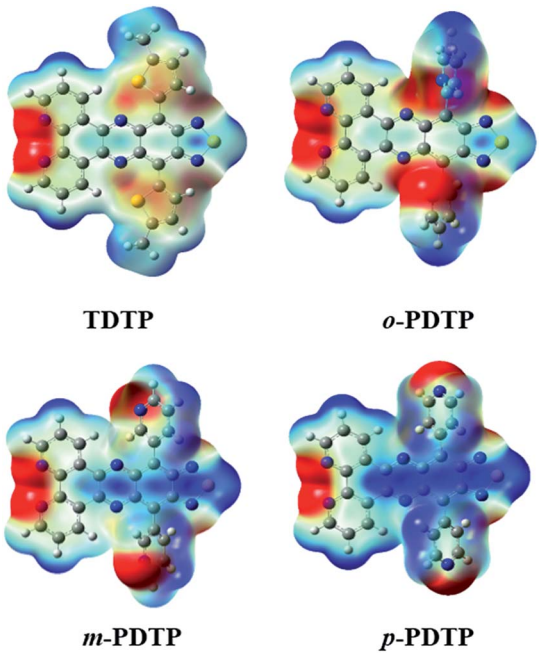


Fig. 5 ESP mapped onto a surface of total electrons for the studied compounds.

attraction mainly appears in the molecular skeleton (left side) of one molecule and the molecular skeleton (right side) of its adjacent molecule, forming the 1D π–π stacking. In *p*-PDTP, the negative potential in the side chains moves to the side chain terminal since nitrogen atoms with strong electronegativity are located there, and accordingly the positive potential also appears in the zone of the side chain near the molecular backbone. As a consequence, besides the attraction between the two sides of the skeleton, there also exists attraction between the molecular skeleton (left side) of one molecule and the molecular skeleton near the side chains of its adjacent molecules, thus resulting in a 2D π–π stacking in *p*-PDTP.

To quantitatively clarify the effect of introducing pyridyl, we calculated the presence of nitrogen atoms in the interaction by the Hirshfeld Surface Analysis (HSA) using CrystalExplorer17.[60,61] The obtained 2D fingerprint plots of the four crystal structure are shown in Fig. 6 and Table 3. The decomposition of the fingerprint plots shows that All···N contacts (all intercontacts involving the nitrogen atom) comprise 12.5% of the total Hirshfeld surface area for the crystal structure of TDTP, while the percentage increases to 17.4%, 17.6%, and 18.1% in

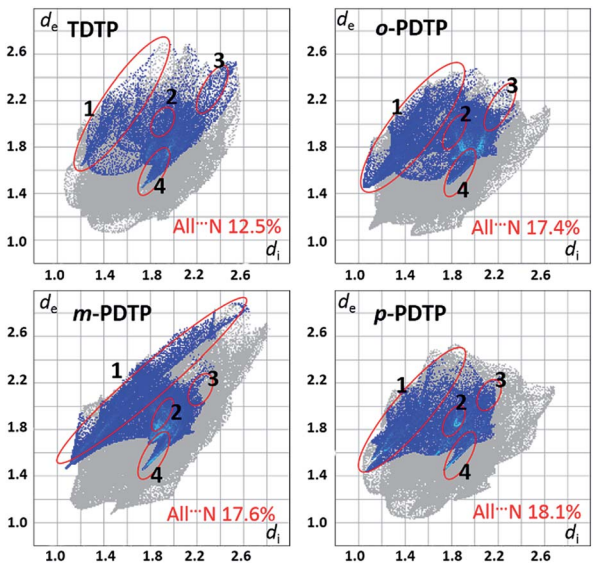


Fig. 6 Fingerprint plots of the studied ETMs: All···N and the resolved percentages of contacts contributing to the Hirshfeld surface area. The H···N, C···N, N···N, and S···N interactions are shown in areas 1, 2, 3, and 4, respectively.

Table 3 Summary of various contacts and their contributions to the Hirshfeld surface of the investigated four crystal structures

| | All···N | H···N | C···N | N···N | S···N |
|---|---|---|---|---|---|
| TDTP | 12.5% | 3.0% | 3.9% | 1.6% | 3.9% |
| *o*-PDTP | 17.4% | 6.5% | 5.1% | 2.7% | 3.1% |
| *m*-PDTP | 17.6% | 7.8% | 4.3% | 1.9% | 3.7% |
| *p*-PDTP | 18.1% | 9.6% | 4.5% | 2.3% | 1.8% |

*o*-PDTP, *m*-PDTP, and *p*-PDTP, respectively. The improved All···N percentage is mainly ascribed to the increase of H···N interaction in PDTPs, that is, the interactions of nitrogen atoms with the neighboring hydrogen atoms. As can be seen in Table 3, the H···N percentage is 3.0% in TDTP, but increases to 6.5% in *o*-PDTP, 7.8% in *m*-PDTP, and 9.6% in *p*-PDTP, meanwhile the percentage changes of other interactions (C···N, N···N, and S···N) are not so manifest. This is consistent with the difference in packing mode.

The electrical anisotropy of organic materials has attracted much attention, due to the fact that it reflects the intrinsic properties.[62] Understanding the anisotropy of the mobility can help control the orientation of the transistor channel relative to the reference axis of the molecular crystal. We investigated the angular dependences of the mobility and plotted the results in Fig. 7. The electron mobility data in all these four single crystals show remarkable anisotropic behavior. In TDTP the direction with the highest electron mobility is along axis *c* of the crystal cell, along which the $\mu$ is 0.093 $cm^2\ V^{-1}\ s^{-1}$, and the smallest electron mobility is along axis *a* with a mobility value of 0.046 $cm^2\ V^{-1}\ s^{-1}$. The highest and the lowest mobilities of 0.035 and 0.016 $cm^2\ V^{-1}\ s^{-1}$ in *o*-PDTP appear at 169° and 79°in the *a*–*c* plane. The highest and the lowest mobilities of 0.102 and 0.045 $cm^2\ V^{-1}\ s^{-1}$ in *m*-PDTP appear at 143° and 53° in the *a*–*c* plane, which are similar to those in TDTP. The highest and the lowest mobilities of 3.063 and 0.869 $cm^2\ V^{-1}\ s^{-1}$ in *p*-PDTP appear at 164° and 73° in the *a*–*b* plane, which are two orders of magnitude higher than that in TDTP.

Based on the above analysis, we can see that introducing pyridyl into TDTP is an effective method to improve electron mobility, due to the fact that the enhanced interactions between nitrogen atoms and hydrogen atoms change the packing mode and increase the transfer integral in corresponding paths.

## Interface properties

The $MAPbI_3$/ETM interface has a deep influence on the electric performance, such as $V_{oc}$, $J_{sc}$, FF, and ultimate PCE.[63] In the simulation of $MAPbI_3$/ETM interface properties, we chose the (110) surface of tetragonal $MAPbI_3$, which was determined as one of the major facets in $MAPbI_3$ by first-principles calculations and powder X-ray diffraction measurements, and thus was often used in similar calculations combined with ETMs.[25,64,65] Both $PbI_2$- and MA-terminated surfaces have been considered, but calculations with the two different terminals provided similar results, so we put the results of the $PbI_2$-terminated surface in the main text (Fig. 8–10) and the results of the MA-terminated surface in the ESI (Fig. ESI4–7†).

As depicted in Fig. 8, in the optimized $MAPbI_3$/ETM structures, the conjugated plane of ETMs is almost parallel to the $MAPbI_3$ surface and the distances between the ETM skeleton to the $MAPbI_3$ surface are estimated to be 3.64, 3.95, 4.76, and 4.39 Å for TDTP, *o*-PDTP, *m*-PDTP, and *p*-PDTP systems, respectively. It should be noted that unlike TDTP in which all atoms of the molecule are almost in one conjugated plane, the newly introduced pyridyl side chains in PDTPs deviate from the main skeleton plane and interact strongly with the perovskite surface, as can be seen in Fig. 8 where the nearest distances between the side chains of PDTPs and the $MAPbI_3$ surface are less than 2.6 Å. In addition, as shown in Fig. ESI3 and ESI5,† the adsorbed ETMs have small effects on the orientation of MA in $MAPbI_3$, where the selected $H_{MA}$–I distances are a little larger in the case of PDTP adsorption than that of TDTP adsorption. This implies

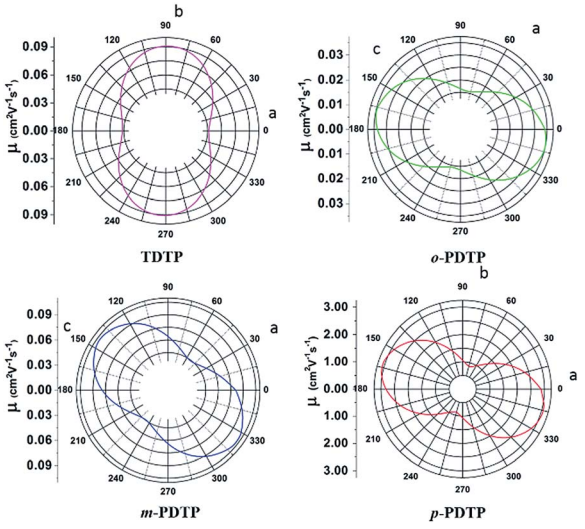


Fig. 7 Calculated mobility anisotropy curve for the investigated crystal structure.

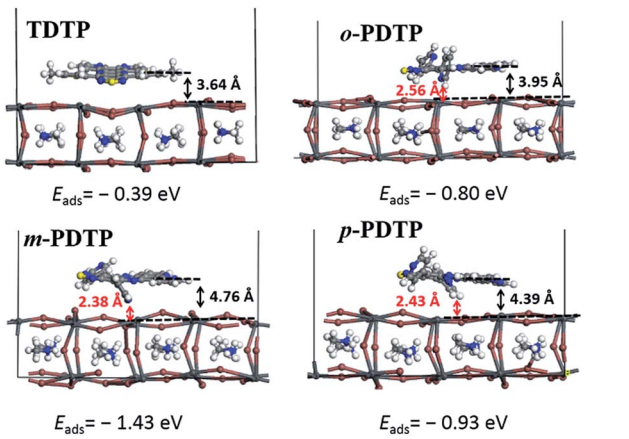


Fig. 8 Optimized structures and binding energies of the ETM on the $PbI_2$-terminated $MAPbI_3$ (110) interface. The arrows indicate the shortest distances between the $MAPbI_3$ surface and the skeleton (in black) or side chain (in red) of the ETM.

enhanced interactions between PDTPs and $MAPbI_3$. The above-mentioned structural features are consistent with the interface adsorption energy ($E_{ads}$) difference, where the $E_{ads}$ absolute values of $MAPbI_3$/PDTPs (0.80–1.43 eV) are much larger than that of $MAPbI_3$/TDTP (0.39 eV). Further analysis shows that the $MAPbI_3$/TDTP interface interaction occurs mainly through the noncovalent bond of lead atoms in $MAPbI_3$ to sulfur atoms in TDTP, while the $MAPbI_3$/PDTP interaction arises mostly from the interaction of the lead atom in $MAPbI_3$ to the nitrogen atom of the introduced pyridyl in PDTPs. Clearly, the $MAPbI_3$/ETM interface interactions are largely enhanced due to the introduction of pyridyl into the ETM.

The $MAPbI_3$/ETM properties were further studied by the analysis of partial density of states (PDOS),[66] see Fig. 9. We need to stress that it is challenging for first-principles calculations to quantitatively reproduce the energy levels by experiments for the combined $MAPbI_3$/ETM system due to imperfections of the calculation methods and the large size of the system.[67] Nevertheless, qualitative results about the effect of introducing pyridyl on the interacting energy levels of the system are valuable. In the $MAPbI_3$/TDTP system, the CBM of $MAPbI_3$ lies above the LUMO energy level of TDTP, ensuring electron injection from $MAPbI_3$ to TDTP, while the VBM of $MAPbI_3$ is slightly lower than the HOMO energy level of TDTP, indicating that the hole also can transfer to TDTP. In this case, the electron and the hole are likely to recombine at the $MAPbI_3$/TDTP interface, leading to the reduction of $J_{sc}$. In the newly designed $MAPbI_3$/PDTP systems, the CBMs (VBMs) of $MAPbI_3$ are larger than the LUMO (HOMO) energy levels of PDTPs, showing suitable interface energy levels that can promote electron injection and prevent hole transfer, associated with the ease of charge separation and the reduction of charge recombination. From this perspective, introducing pyridyl into TDTP is beneficial for the improvement of $J_{sc}$. Note that the $E_{HOMO}$ value of isolated TDTP is 0.27 eV lower than the VBM of $MAPbI_3$ (see Fig. 3), while the VBM of $MAPbI_3$ is slightly lower than the HOMO energy level of TDTP in the $MAPbI_3$/TDTP system (see Fig. 9). This point shows the importance and necessity of studying the interface properties rather than isolated molecules, because the weak interactions between $MAPbI_3$ and the ETM in the $MAPbI_3$/ETM system result in charge redistribution, which leads to the formation of the interfacial electric dipole and the shift of energy levels. Similar situations were also found in previous studies.[68–71]

In order to explore the separation of electrons and holes, the charge density difference (CDD) pictures of the $MAPbI_3$/ETM systems are depicted in Fig. 10, where the charge depletion and charge accumulation are denoted by yellow color and blue color, respectively. Clearly, significant charge redistributions occur around the interface between $MAPbI_3$ and the ETMs. Different from the $MAPbI_3$/TDTP interface where charge depletion and accumulation mainly appear in the region of interaction between S in the ETM and Pb in $MAPbI_3$, at the $MAPbI_3$/PDTP interface, the charge redistributions appear in both the region of S···Pb interaction and the region of N···Pb interaction, suggesting that the N···Pb interaction plays an important role in electron transfer at the interface. According to the plane-integrated electron density difference along the $z$ direction (the right column in Fig. 10), the electron accumulation ($\Delta\rho < 0$ region) mainly takes place in the conjugated plane of TDTP in the $MAPbI_3$/TDTP system, while the electron accumulation occurs in both the PDTP skeleton and the side chain of pyridyl in PDTPs/$MAPbI_3$ systems, illustrating that the added pyridyl group takes part in electron transfer from $MAPbI_3$ to PDTP.[72–74] Further charge analysis based on Bader charge analysis[75] shows that the numbers of transferred electrons from

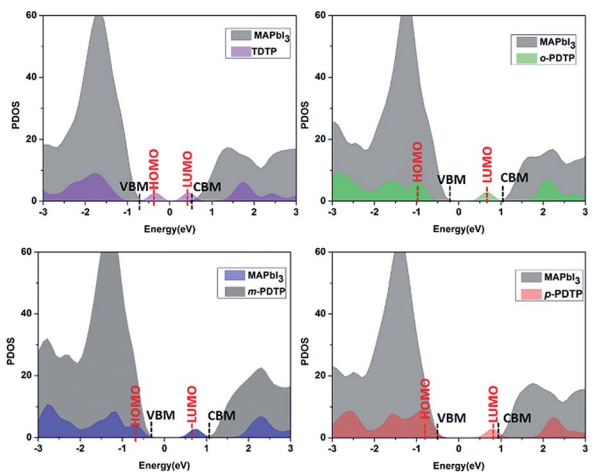


Fig. 9 Partial density of states (PDOS) with summed contributions from ETMs and $MAPbI_3$ for the $PbI_2$-terminated $MAPbI_3$ (110)/ETM interface. The HOMO and LUMO energy levels of ETMs and the VBM and CBM of $MAPbI_3$ are also shown.

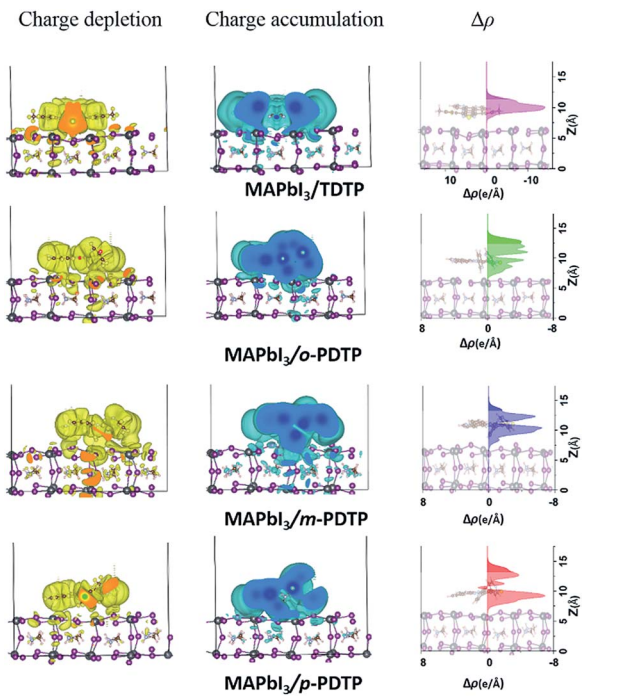


Fig. 10 Electron charge density difference (the left and middle columns) and plane-integrated electron density difference along the $z$ direction (the right column) for the studied ETMs on the $PbI_2$-terminated $MAPbI_3$ (110) surface with an isovalue of $1 \times 10^{-4}$ e $Å^{-1}$.

$MAPbI_3$ to ETMs are 0.48, 0.50, 0.39, and 0.39 electrons for TDTP, *o*-PDTP, *m*-PDTP and *p*-PDTP adsorbed on $MAPbI_3$ systems.

## Conclusions

In this work, we have designed a series of ETMs (*o*-PDTP, *m*-PDTP, and *p*-PDTP) through introducing pyridyl into the TDTP molecule and investigated the energy levels and electron transfer properties of isolated ETMs and the $MAPbI_3$/ETM interface properties. The newly designed PDTPs exhibit appropriate energy levels matched with $MAPbI_3$, and larger band gaps compared with TDTP. In respect of electron transfer, the average mobility of *p*-PDTP is up to 1.65 $cm^2 V^{-1} s^{-1}$, which is 34 times higher than that of TDTP. The enhanced electron mobility is attributed to the packing mode change from the herringbone packing motif in TDTP to the 2D π–π stacking in *p*-PDTP. Moreover, the PDTPs possess better air solubility and solubility than TDTP. The obtained $MAPbI_3$/ETM interface properties demonstrate that introducing pyridyl is favorable for improving electron transfer from $MAPbI_3$ to ETMs and decreases charge recombination, which may help to enhance the short-circuit current. Therefore, the newly designed *m*-PDTP and *p*-PDTP could be used as efficient ETMs in inverted PSCs, and the method of introducing pyridyl into ETMs could be a design strategy for future experiments.

## Conflicts of interest

There are no conflicts to declare.

## Acknowledgements

This work is financially supported by the National Natural Science Foundation of China (21473010 and 21773007), and Beijing Key Laboratory for Chemical Power Source and Green Catalysis (2013CX02031). We thank associate professor Li-jie Li for the code to predict the crystal structure.

## Notes and references

1 Q. Wang, Y. Shao, Q. Dong, Z. Xiao, Y. Yuan and J. Huang, *Energy Environ. Sci.*, 2014, **7**, 2359–2365.
2 Y. Bai, Q. Dong, Y. Shao, Y. Deng, Q. Wang, L. Shen, D. Wang, W. Wei and J. Huang, *Nat. Commun.*, 2016, **7**, 12806.
3 T. Liu, K. Chen, Q. Hu, R. Zhu and Q. Gong, *Adv. Energy Mater.*, 2016, **6**, 1600457.
4 S. K. Jung, J. H. Heo, D. W. Lee, S. H. Lee, S. C. Lee, W. Yoon, H. Yun, D. Kim, J. H. Kim, S. H. Im and O. P. Kwon, *ChemSusChem*, 2019, **12**, 224–230.
5 C. Chen, H. Li, X. Ding, M. Cheng, H. Li, L. Xu, F. Qiao, H. Li and L. Sun, *ACS Appl. Mater. Interfaces*, 2018, **10**, 38970–38977.
6 I. M. Hermes, Y. Hou, V. W. Bergmann, C. J. Brabec and S. A. L. Weber, *J. Phys. Chem. Lett.*, 2018, **9**, 6249–6256.
7 W. Wang, J. Yuan, G. Shi, X. Zhu, S. Shi, Z. Liu, L. Han, H. Q. Wang and W. Ma, *ACS Appl. Mater. Interfaces*, 2015, **7**, 3994–3999.
8 S.-K. Jung, D. S. Lee, M. H. Ann, S. H. Im, J. H. Kim and O. P. Kwon, *ChemSusChem*, 2018, **11**, 3882–3892.
9 K. Liu, S. Dai, F. Meng, J. Shi, Y. Li, J. Wu, Q. Meng and X. Zhan, *J. Mater. Chem. A*, 2017, **5**, 21414–21421.
10 L. Zhu, C. Song, X. Li, Y.-C. Wang, W. Zhang, X. Sun, W. Zhang and J. Fang, *J. Mater. Chem. C*, 2017, **5**, 10777–10784.
11 Z. Zhu, D. Zhao, C.-C. Chueh, X. Shi, Z. Li and A. K. Y. Jen, *Joule*, 2018, **2**, 168–183.
12 J. Jiang, Z. Jin, J. Lei, Q. Wang, X. Zhang, J. Zhang, F. Gao and S. Liu, *J. Mater. Chem. A*, 2017, **5**, 9514–9522.
13 M. Ye, C. He, J. Iocozzia, X. Liu, X. Cui, X. Meng, M. Rager, X. Hong, X. Liu and Z. Lin, *J. Phys. D: Appl. Phys.*, 2017, **50**, 373002.
14 Y. Zhang, P. Wang, X. Yu, J. Xie, X. Sun, H. Wang, J. Huang, L. Xu, C. Cui, M. Lei and D. Yang, *J. Mater. Chem. A*, 2016, **4**, 18509–18515.
15 N. Wang, K. Zhao, T. Ding, W. Liu, A. S. Ahmed, Z. Wang, M. Tian, X. W. Sun and Q. Zhang, *Adv. Energy Mater.*, 2017, **7**, 1700522.
16 J.-l. Wu, W.-K. Huang, Y.-C. Chang, B.-C. Tsai, Y.-C. Hsiao, C.-Y. Chang, C.-T. Chen and C.-T. Chen, *J. Mater. Chem. A*, 2017, **5**, 12811–12821.
17 Y. Li, K. Lu, X. Ling, J. Yuan, G. Shi, G. Ding, J. Sun, S. Shi, X. Gong and W. Ma, *J. Mater. Chem. A*, 2016, **4**, 10130–10134.
18 D. B. Shaikh, A. A. Said, R. S. Bhosale, W. Chen, S. V. Bhosale, A. L. Puyad, S. V. Bhosale and Q. Zhang, *Asian J. Org. Chem.*, 2018, **7**, 2294–2301.
19 J.-T. Shieh, C.-H. Liu, H.-F. Meng, S.-R. Tseng, Y.-C. Chao and S.-F. Horng, *J. Appl. Physiol.*, 2010, **107**, 084503.
20 L. Yan, Y. Zhao, H. Yu, Z. Hu, Y. He, A. Li, O. Goto, C. Yan, T. Chen, R. Chen, Y.-L. Loo, D. F. Perepichka, H. Meng and W. Huang, *J. Mater. Chem. C*, 2016, **4**, 3517–3522.
21 M. J. Kim, Y. W. Lee, Y. Lee, H. Y. Woo and J. Ho Cho, *J. Mater. Chem. C*, 2018, **6**, 5698–5706.
22 Y. H. Wu, X. Q. Shi, X. H. Ding, Y. K. Ren, T. Hayat, A. Alsaedi, Y. Ding, P. Xu and S. Y. Dai, *ACS Appl. Mater. Interfaces*, 2018, **10**, 3602–3608.
23 Y. Shi, X. Wang, H. Zhang, B. Li, H. Lu, T. Ma and C. Hao, *J. Mater. Chem. A*, 2015, **3**, 22191–22198.
24 F. Han, G. Hao, Z. Wan, J. Luo, J. Xia and C. Jia, *Electrochim. Acta*, 2019, **296**, 75–81.
25 B. Li, J. Zhen, Y. Wan, X. Lei, Q. Liu, Y. Liu, L. Jia, X. Wu, H. Zeng, W. Zhang, G. W. Wang, M. Chen and S. Yang, *ACS Appl. Mater. Interfaces*, 2018, **10**, 32471–32482.
26 B. Wang, G. Mu, J. Tan, Z. Lei, J. Jin and L. Wang, *J. Mater. Chem. C*, 2015, **3**, 7709–7719.
27 C. J. Mueller, C. R. Singh, M. Fried, S. Huettner and M. Thelakkat, *Adv. Funct. Mater.*, 2015, **25**, 2725–2736.
28 H. Ye, D. Chen, M. Liu, S.-J. Su, Y.-F. Wang, C.-C. Lo, A. Lien and J. Kido, *Adv. Funct. Mater.*, 2014, **24**, 3268–3275.
29 G. Qiu, Z. Jiang, Z. Ni, H. Wang, H. Dong, J. Zhang, X. Zhang, Z. Shu, K. Lu, Y. Zhen, Z. Wei and W. Hu, *J. Mater. Chem. C*, 2017, **5**, 566–572.

30 L. Meng, J. You, T. F. Guo and Y. Yang, *Acc. Chem. Res.*, 2016, **49**, 155–165.
31 P.-Y. Gu, N. Wang, C. Wang, Y. Zhou, G. Long, M. Tian, W. Chen, X. W. Sun, M. G. Kanatzidis and Q. Zhang, *J. Mater. Chem. A*, 2017, **5**, 7339–7344.
32 W. S. Yang, B.-W. Park, E. H. Jung, N. J. Jeon, Y. C. Kim, D. U. Lee, S. S. Shin, J. Seo, E. K. Kim, J. H. Noh and S. I. Seok, *Science*, 2017, **356**, 1376.
33 D. Zhao, Z. Zhu, M. Y. Kuo, C. C. Chueh and A. K. Jen, *Angew. Chem., Int. Ed.*, 2016, **55**, 8999–9003.
34 P. Tiwana, P. Docampo, M. B. Johnston, H. J. Snaith and L. M. Herz, *ACS Nano*, 2011, **5**, 5158–5166.
35 Y. Zhang, Y. Duan, J. Liu, D. Zheng, M. Zhang and G. Zhao, *J. Phys. Chem. C*, 2017, **121**, 17633–17640.
36 W.-J. Chi, P.-P. Sun and Z.-S. Li, *Phys. Chem. Chem. Phys.*, 2016, **18**, 27073–27077.
37 R. Zhu, Q.-S. Li and Z.-S. Li, *Nanoscale*, 2018, **10**, 17873–17883.
38 G. Zhang and C. B. Musgrave, *J. Phys. Chem. A*, 2007, **111**, 1554–1561.
39 J. Chang, J. Xiao, Z. Lin, H. Zhu, Q.-H. Xu, K. Zeng, Y. Hao and J. Ouyang, *J. Mater. Chem. A*, 2016, **4**, 17464–17472.
40 S. K. Jung, D. S. Lee, M. H. Ann, S. H. Im, J. H. Kim and O. P. Kwon, *ChemSusChem*, 2018, **11**, 3882–3892.
41 H.-S. Kim, J.-Y. Seo and N.-G. Park, *ChemSusChem*, 2016, **9**, 2528–2540.
42 J. H. Heo, S.-C. Lee, S.-K. Jung, O. P. Kwon and S. H. Im, *J. Mater. Chem. A*, 2017, **5**, 20615–20622.
43 Y.-C. Chang, M.-Y. Kuo, C.-P. Chen, H.-F. Lu and I. Chao, *J. Phys. Chem. C*, 2010, **114**, 11595–11601.
44 M. Y. Kuo, H. Y. Chen and I. Chao, *Chemistry*, 2007, **13**, 4750–4758.
45 M. S. Stark, *J. Phys. Chem. A*, 1997, **101**, 8296–8301.
46 M. Liu, M. B. Johnston and H. J. Snaith, *Nature*, 2013, **501**, 395–398.
47 M. M. Lee, J. Teuscher, T. Miyasaka, T. N. Murakami and H. J. Snaith, *Science*, 2012, **338**, 643.
48 J. Ho, A. Klamt and M. L. Coote, *J. Phys. Chem. A*, 2010, **114**, 13442–13444.
49 H. Oberhofer, K. Reuter and J. Blumberger, *Chem. Rev.*, 2017, **117**, 10319–10357.
50 Y. L. Niu, W. Q. Li, Q. Peng, H. Geng, Y. P. Yi, L. J. Wang, G. J. Nan, D. Wang and Z. G. Shuai, *Mol. Phys.*, 2018, **116**, 1078–1090.
51 G. Nan, X. Yang, L. Wang, Z. Shuai and Y. Zhao, *Phys. Rev. B: Condens. Matter Mater. Phys.*, 2009, **79**, 115203.
52 W.-C. Chen and I. Chao, *J. Phys. Chem. C*, 2014, **118**, 20176–20183.
53 R. Zhu, Y.-A. Duan, Y. Geng, C.-Y. Wei, X.-Y. Chen and Y. Liao, *Comput. Theor. Chem.*, 2016, **1078**, 16–22.
54 L. F. Ji, J. X. Fan, S. F. Zhang and A. M. Ren, *Phys. Chem. Chem. Phys.*, 2017, **19**, 13978–13993.
55 V. Coropceanu, J. Cornil, D. A. da Silva Filho, Y. Olivier, R. Silbey and J.-L. Brédas, *Chem. Rev.*, 2007, **107**, 926–952.
56 I. One, *Molecular Simulation Software*, https://www.accelrys.com.
57 A. Irfan, A. G. Al-Sehemi and A. Kalam, *J. Mol. Struct.*, 2013, **1049**, 198–204.
58 J. C. Sancho-García and A. J. Pérez-Jiménez, *Chem. Phys. Lett.*, 2010, **499**, 146–151.
59 S. E. Wheeler and K. N. Houk, *J. Chem. Theory Comput.*, 2009, **5**, 2301–2312.
60 M. J. Turner, J. J. McKinnon, S. K. Wolff, D. J. Grimwood, P. R. Spackman, D. Jayatilaka and M. A. Spackman, *Crystal Explorer17*, University of Western Australia, 2017, http://hirshfeldsurface.net.
61 J. J. McKinnon, D. Jayatilaka and M. A. Spackman, *Chem. Commun.*, 2007, 3814–3816.
62 S. Wen, W. Q. Deng and K. L. Han, *Chem. Commun.*, 2010, **46**, 5133–5135.
63 L. X. Shi, Z. S. Wang, Z. Huang, W. E. I. Sha, H. Wang and Z. Zhou, *AIP Adv.*, 2018, **8**, 025312.
64 S. Colella, E. Mosconi, G. Pellegrino, A. Alberti, V. L. Guerra, S. Masi, A. Listorti, A. Rizzo, G. G. Condorelli, F. De Angelis and G. Gigli, *J. Phys. Chem. Lett.*, 2014, **5**, 3532–3538.
65 J. H. Heo, S. H. Im, J. H. Noh, T. N. Mandal, C.-S. Lim, J. A. Chang, Y. H. Lee, H.-j. Kim, A. Sarkar, M. K. Nazeeruddin, M. Grätzel and S. I. Seok, *Nat. Photonics*, 2013, **7**, 486.
66 Q. Tang, Z. Zhou and P. Shen, *J. Am. Chem. Soc.*, 2012, **134**, 16909–16916.
67 E. Mosconi, E. Ronca and F. De Angelis, *J. Phys. Chem. Lett.*, 2014, **5**, 2619–2625.
68 R. Lindblad, D. Bi, B. W. Park, J. Oscarsson, M. Gorgoi, H. Siegbahn, M. Odelius, E. M. Johansson and H. Rensmo, *J. Phys. Chem. Lett.*, 2014, **5**, 648–653.
69 H. Ishii, K. Sugiyama, E. Ito and K. Seki, *Adv. Mater.*, 1999, **11**, 605–625.
70 J. Yin, D. Cortecchia, A. Krishna, S. Chen, N. Mathews, A. C. Grimsdale and C. Soci, *J. Phys. Chem. Lett.*, 2015, **6**, 1396–1402.
71 G. Xing, B. Wu, S. Chen, J. Chua, N. Yantara, S. Mhaisalkar, N. Mathews and T. C. Sum, *Small*, 2015, **11**, 3606–3613.
72 C. Xia, J. Du, W. Xiong, Y. Jia, Z. Wei and J. Li, *J. Mater. Chem. A*, 2017, **5**, 13400–13410.
73 J. Yin, D. Cortecchia, A. Krishna, S. Chen, N. Mathews, A. C. Grimsdale and C. Soci, *J. Phys. Chem. Lett.*, 2015, **6**, 1396–1402.
74 M. Bokdam, P. A. Khomyakov, G. Brocks, Z. Zhong and P. J. Kelly, *Nano Lett.*, 2011, **11**, 4631–4635.
75 E. Sanville, S. D. Kenny, R. Smith and G. Henkelman, *J. Comput. Chem.*, 2007, **28**, 899–908.

 